PCCP

Accepted Manuscript

ROYAL SOCIETY OF CHEMISTRY

www.rsc.org/pccp

Mechanism of Anisotropic Surface Self-Diffusivity at the Prismatic Ice-Vapor Interface

Ivan Gladich[1,*], Amrei Oswald[2], Natalie Bowens[2], Sam Naatz[2], Penny Rowe[3,4], Martina Roeselova[5], and Steven Neshyba[2,*]

[1]Qatar Environment and Energy Research Institute, P.O. Box 5825, Doha, Qatar
[2]University of Puget Sound, 1500 N. Warner, Tacoma, Washington, USA
[3]Universidad de Santiago de Chile, Ave Bernardo O'Higgins 3363, Santiago, Chile
[4]Geography Department, University of Idaho, Moscow, Idaho, USA
[5]Institute of Organic Chemistry and Biochemistry, Academy of Sciences of the Czech Republic, Flemingovo nám. 2 16610 Prague 6 Czech Republic

*Corresponding authors:
Ivan Gladich: igladich@qf.org.qa
Steven Neshyba: nesh@pugetsound.edu

MECHANISM OF ANISOTROPIC SURFACE SELF-DIFFUSIVITY AT THE PRISMATIC ICE-VAPOR INTERFACE

Abstract

Predictive theoretical models for mesoscopic roughening of ice require improved understanding of attachment kinetics occurring at the ice-vapor interface. Here, we use classical molecular dynamics to explore the generality and mechanics of a transition from anisotropic to isotropic self-diffusivity on exposed prismatic surfaces. We find that self-diffusion parallel to the crystallographic a-axis is favored over the c-axis at sub-melt temperatures below about -35°C, for three different representations of the water-water intermolecular potential. In the low-temperature anisotropic regime, diffusion results from interstitial admolecules encountering entropically distinct barriers to diffusion in the two in-plane directions. At higher temperatures, isotropic self-diffusion occurring deeper within the quasi-liquid layer becomes the dominant mechanism, owing to its larger energy of activation.

Key words

ice, diffusion, anisotropy, molecular dynamics

1. Introduction

Mesoscopic (micrometer-scale) roughening of the surfaces of ice crystals in cirrus clouds is known to modify the light-scattering properties of these clouds in significant ways,[1–6] but incorporation of realistic roughening in radiative transfer models is hampered by incomplete understanding of how this roughening arises. A predictive theoretical model for mesoscopic roughening, in turn, requires a firmer understanding of the relevant atomistic processes occurring at the ice-vapor interface.

It is widely accepted that microscopic structure of crystalline surfaces can have macroscopic effects.[7] In the case of growing ice, for example, growth rates and hence ice crystal shape are a strong function of microscopic structure at facet surfaces.[8,9] However, application of these ideas to mesoscopic roughening in atmospheric ice presents significant challenges, in large part because the diversity of conditions encountered in remote-sensing measurements of atmospheric ice has led to myriad and sometimes contradictory observations. As falling cirrus ice crystals pass through atmospheric layers of higher temperature, investigators have observed enhanced attenuation of backscattered light and attributed it to more pronounced mesoscopic roughening.[10] Other investigators have reported that mesoscopic roughening becomes more pronounced with *decreasing* temperature, however,[11] while still others have found evidence that roughness depends on the "history of supersaturation" (including ablation) experienced by ice crystals.[12]

Optical and other forms of microscopy have, nevertheless, produced abundant evidence of microscopic effects on mesoscopic structure.[13] Of the facets occurring in atmospheric ice (Fig. 1a), six-fold roughening symmetry is frequently seen on exposed basal facets (Fig. 1b), and two-fold roughening symmetry is frequently seen on cold (by tropospheric standards) prismatic facets (Fig. 1c). Two-fold roughening symmetry in prismatic facets has also been documented in laboratory-grown ice using scanning electron microscopy.[11,13–16]

These considerations lead us to seek a theoretical model capable of generating mesoscopic roughening that is affected by microscopic structure, and to identify conditions under which it may be applicable. Such a model has emerged in the context of metal epitaxy;[18] we will refer to it here as the epitaxial island model. The starting point is classical two-dimensional layer nucleation theory, in which an exposed crystalline facet populated by weakly bound atoms or molecules ("admolecules") develops embryonic monomolecular thick islands.[19] Once such islands form, they grow laterally because of attachment of other admolecules at their edges. Mesoscopic symmetry emerges, in this model, when attachment is affected by the underlying crystal lattice symmetry. Mechanisms by which this could occur include anisotropic self-diffusivity in the plane of the facet, and symmetry-dependent stickiness of island edges. Both have been used to account for mesoscopic roughness observed on metal facets.[18]

The epitaxial island model, therefore, offers a framework for predicting the symmetry of mesoscopic roughening based on atomistic structure and surface kinetics. Is the model appropriate for ice facets? A complicating factor is the presence of a quasi-liquid layer (QLL), the thickness of which changes with temperature. Exploring the applicability of

the epitaxial island model for water ice therefore requires proper representation of motion of molecules within the QLL.

Molecular dynamics (MD) is a useful method for exploring questions such as this.[20–26] From MD simulations of diffusion on the (110) surface of face-centered-cubic metals, for example, anisotropic diffusion of admolecules atop this surface was attributed to the existence of two distinct diffusion mechanisms in the two in-plane directions: uncorrelated jump diffusion in one direction, and correlated exchange in the other.[27,28] MD simulations of self-diffusion at exposed basal surfaces of ice have demonstrated that the QLL plays a dominant role in surface self-diffusion, and that at sub-melting temperatures lower than -35 □C this diffusivity is anisotropic[15,17,20,22] (the sub-melting temperature is defined as the nominal temperature minus the model's empirically determined melting temperature, $T_s = T - T_m$). Low-temperature anisotropic diffusivity, moreover, has been found to give way to isotropic diffusivity at elevated temperatures (hereafter, an anisotropic-to-isotropic transition, or AI transition), although so far this has been documented only for a single water-water intermolecular potential (the six-site NE6 model[29]).

Here, we report progress toward the goal of elucidating the atomistic processes that influence mesoscopic roughness at the ice-vapor interface, with a particular focus on the AI transition. We first evaluate the generality of diffusive anisotropy at the prismatic ice-vapor interface by carrying out classical MD simulations employing two representations of the water-water intermolecular potential in addition to the NE6 model used in prior work.[17] We then explore the mechanism underlying anisotropic diffusivity by analysis of thousands of discrete, single-molecule diffusion events, in which molecules jump from position to position atop the quasi-liquid surface on a picosecond timescale. We also examine the distribution of admolecules atop a relatively rigid sub-layer of other molecules comprising the QLL, and the kinetics implied by that distribution. We conclude with a proposed mechanism for the AI transition that accounts for these observations.

2. Methods

2.1 Molecular dynamics simulations

The anisotropy of water self-diffusivity on the prismatic ice surface was investigated in previous work using classical MD simulations employing the NE6 water model[29]. Here, we performed classical MD simulations of the prismatic ice–vapor interface using two other water force fields, TIP4P/2005 (ref. 30) and TIP5P-Ew (ref. 31). While the NE6 force field was developed specifically for simulations of water ice, the other two force fields have also been shown to provide a reliable description of ice properties[15,17,32–35], and they are widely used for ice simulations. TIP4P/2005 is a four-site water model that was designed to properly describe the water phase diagram and, thus, to correctly reproduce the liquid water-ice coexistence. As a result of the "universal" character of the TIP4P/2005 model, i.e., its applicability under a broad range of conditions, the model under-predicts the melting temperature of hexagonal ice (I_h) at atmospheric pressure, yielding $T_m = 252$ K (refs. 30,36). The five-site TIP5P-Ew model yields poorer

performance in terms of the overall phase diagram and slightly over-predicts the stability of ice II compared to the hexagonal ice Ih[37,38]. On the other hand, the TIP5P-Ew ice Ih melting temperature is 272 K (ref. 36), very close to the experimental one. The melting point of the NE6 force field, used in our previous MD simulations[17], is 289 K (ref. 39), resulting in NE6 ice being stable up to ~16 °C above the experimental melting temperature of hexagonal ice. The water parameters and corresponding melting temperatures are reported in Tables 1 and 2, respectively. All of the above models satisfactorily reproduce water diffusivity in the bulk liquid supercooled regime[31,32,40,41].

For MD simulations with the TIP4P/2005 and TIP5P-Ew force fields, equilibrated ice slabs with two vapor/ice interfaces were prepared using the same system size and following the same procedure as in our previous work, in which the NE6 force field was employed[17]. The algorithm of Buch et al.[42] was used to construct an initial proton disordered ice Ih crystal having a slab thickness of 24 layers in the x-direction, 12 bilayers in the y-direction, and 10 bilayers in the z-direction, for a total of 2880 water molecules. The dimensions of the ice sample were approximately 5.4 nm (x) × 4.7 nm (y) × 3.7 nm (z), and Cartesian periodic boundary conditions were used. Starting from this configuration, the TIP4P/2005 ice crystal was heated to the target temperatures of 192, 202, 212, 222, 232, 242, and 250 K, whereas the TIP5P-Ew ice crystal was heated to 212, 222, 232, 242, 252, 262, and 270 K. For TIP4P/2005 and TIP5P-Ew, the nominal temperatures correspond to sub-melting temperatures T_s = -60, -50, -40, -30, -20, -10, and -2 °C, comparable to the sub-melting temperatures used in our previous work with the NE6 water model.[17] The heating process consisted in linearly increasing the temperature of the ice crystal from 0 K to each of the target temperatures in a constant-pressure simulation over the course of 1.5 ns, followed by another 1 ns equilibration at the target temperature in an isobaric-isothermal (NpT) simulation. During the heating and equilibration, a small time step of 0.1 fs was used to allow for the adjustment of the ice crystal structure to the temperature increase, thus avoiding ice crystal disorder and melting. Next, the barostat was set to zero pressure[43]. Upon equilibrating the bulk ice samples to the desired temperatures, the y-dimension of each of the simulation cells of the equilibrated ice systems was elongated to 14 nm, resulting in "freshly cleaved" slabs of ice with two primary prismatic facets $(10\bar{1}0)$ exposed to the vacuum. From these initial configurations, isochoric and isothermal (NVT) simulations at each of the target temperature were run for 200 ns with a time steps of 2 fs, saving the system configuration every 1 ps. The NE6 trajectories, taken from our previous work,[17] consisted of 100 ns. In order to rule out any possible periodic boundary condition artifact due to the rectangular interface in the XZ plane, we also built a second ice crystal with dimensions 4.4 nm (x) × 4.7 nm (y) × 4.5 nm (z), consisting of 20 layers, 12 bilayers, and 12 bilayers in the x, y and z-directions, respectively. Starting from this crystal, an ice slab, designated here NE6(sq), was constructed according to the same procedure described above.

All simulations were performed in double precision floating point format with GROMACS 4.5.4 (ref. 44) using the leap-frog integration scheme.[45,46] In accord with the original parameterization of TIP4P/2005 (ref. 30) and TIP5P-Ew (ref. 31), we used a cut-off of 0.9 nm for the van der Waals and the real-space parts of the Coulomb interactions, updating the neighbor list every integration step. The long-range part of the Coulomb

interaction was calculated by the particle-mesh Ewald method[46,47], using a relative tolerance of 10^{-5}, fourth-order cubic interpolation and 0.12 Fourier spacing. The canonical velocity-rescaling thermostat[48] with a time constant of 0.1 ps was used to control the temperature. During the NpT equilibration runs, the pressure was controlled by the Parinello-Rahman barostat[49] with a coupling time of 2 ps. Finally, water molecule geometry was constrained using the SETTLE algorithm[50]. This numerical set-up was tested in terms of total energy conservation and numerical performance in our previous work, the only difference being the cut-off of 1.0 nm employed in the simulations in the previous work with the NE6 model.[17]

2.2 Calculation of surface diffusivity

To evaluate the anisotropy of water self-diffusivity on the prismatic ice surface at each temperature, in-plane displacements atop the $(10\bar{1}0)$ facet were measured. These in-plane directions are designated x (for motion perpendicular to the $(11\bar{2}0)$ facet) and z (for motion perpendicular to the (0001) facet), as shown in Fig. 1. Diffusion coefficients were deduced from the slopes of the corresponding one-dimensional mean-squared displacement (MSD) using the Einstein relation,

$$D_s = \frac{1}{2}\frac{dMSD_s(t)}{dt} \quad (1)$$

where coordinate *s* here refers *x* or *z* in Fig. 1a. Calculations of MSD at different temperatures were performed using the GROMACS utility g_msd.[44] The initial 4 ns of the 100 ns trajectories were discarded to allow for the formation of a well-equilibrated disordered quasi-liquid layer on the two prismatic ice-vapor interfaces of the ice slab. For each trajectory, multiple MSD plots were computed advancing the starting time in 20 ps intervals and, eventually, averaging over all the obtained MSD plots. Diffusion coefficients were then computed from the slope of the linear fit of the most statistically relevant part of the averaged MSD plot, which was determined to be between 5 and 25 ns. Water molecules that sublimated from the ice surface during the simulation were excluded from the computation of the MSD.

For comparison with bulk diffusivity values, MSD functions were scaled to take into account the number of crystalline ice water molecules that are immobile. Molecules identified as liquid-like were assumed to be mobile, whereas it was assumed that those that are embedded in the ice crystal lattice do not contribute to the lateral surface diffusivity. Molecules embedded in the ice crystal lattice were identified as tetrahedrally coordinated. For each water molecule in the system, denoted by the index *i*, the tetrahedral order parameter value, q_i, of Errington and Debenedetti[51] was assigned:

$$q_i = \left[1 - \frac{3}{8}\sum_{j=1}^{3}\sum_{k=j+1}^{4}\left(\cos(\theta_{i,j,k}) + \frac{1}{3}\right)^2\right]. \quad (2)$$

Equation 2 is calculated by summing the angular positions (θ) of the four nearest neighbor oxygen atoms (indices j and k) with respect to the oxygen atom of the i^{th} water

molecule. This procedure yields a q_i value close to 1 for water molecules belonging to the bulk ice phase (with a close-to-ideal tetrahedral coordination), while lower q_i values are assigned to the liquid phase. Based on that, it is possible to define a threshold, q_t, such that for $q_i > q_t$ a water molecule is assigned to the crystal ice phase, whereas for $q_i < q_t$ the molecule is identified as liquid-like. Values of q_t for the TIP4P/2005 and TIP5P-Ew water models have been calculated previously as 0.9054 and 0.9257, respectively[52]. The above procedure allows identification of liquid-like water molecules in each trajectory frame. By averaging over the trajectory, the mean number of liquid-like water molecules in the system can be calculated.

The resulting one-dimensional surface diffusivity, D_s^*, is given by

$$D_s^* = D_s/Q \tag{3}$$

where Q is the ratio of the average number of liquid like molecules, N_{LL}, to the total number of water molecules present in the system (2880), neglecting the evaporated ones, N_{EV},

$$Q = \frac{(N_{LL} - N_{EV})}{(2880 - N_{EV})} \tag{4}$$

Finally, a two-dimensional surface diffusivity can be calculated from the one-dimensional diffusivities as

$$D_{x,z}^* = \left(D_x^* + D_z^*\right)/2 \tag{5}$$

It should be noted that while absolute values of D_s^* depend on Q, *ratios* of diffusivity at any given temperature do not: $\frac{D_x^*}{D_z^*} = \frac{D_x}{D_z}$. Hence inferences about anisotropic diffusion derived from these ratios are not subject to the choice of criterion used to discriminate between liquid-like and ice-like molecules.

2.3 Automated identification of discrete diffusion events

Statistics of discrete diffusion events were obtained from NE6 trajectories at a temperature of 230 K. A robust computational method was devised for automating the identification of discrete diffusion events in these trajectories. This algorithm was applied separately to the position of each water molecule in each Cartesian direction, as follows (in the steps given below, coordinate s refers x, y, or z in Fig. 1a).

1. A five-picosecond running mean of s, designated s' was obtained.
2. Intervals of time $(t_{initial}, t_{final})$ where $\left|\frac{ds'}{dt}\right| \geq \left|\frac{ds'}{dt}\right|_{crit}$ were identified (see description of $\left|\frac{ds'}{dt}\right|_{crit}$ below).
3. Intervals separated from one another by less than 5 ps were combined into a single

interval (this is to avoid counting the large oscillations that tend to precede and follow diffusion events as multiple events).

4. If $\left|s\left(t_{final}+3\ ps\right)-s(t_{initial}-3\ ps)\right|>\Delta s_{crit}$, the interval was designated as a discrete diffusion event, and the instantaneous positions recorded.

The threshold values $\left|\frac{ds'}{dt}\right|_{crit}$ and Δs_{crit} are chosen to be small enough to capture interstitial motions (as well as larger motions), but large enough to exclude small displacements judged to be due to thermal motion within local potential energy minima. Threshold values $\left|\frac{ds'}{dt}\right|_{crit}=0.015$ nm/ps and $\Delta s_{crit}=0.05$ nm accomplish this purpose.

As an example of the application of these steps, Fig. 2 (upper panel) shows the trajectory of a water molecule in the x-direction (blue) along with the running average x' (red), and the derivative computed in the first step of our algorithm, $\frac{dx'}{dt}$. The interval $(25.127\ \text{ns}, 25.133\ \text{ns})$ was identified as a potential discrete diffusion event since, in this interval, the slope (lower panel of Fig. 2) exceeded the threshold value of 0.015. Broadening the window by ±0.003 ns at each end (as indicated by the black boxes on the left hand side of Fig. 2), we find the displacement to be

$$|\,\Delta x\,|\ =0.19\ \text{nm}$$

As this displacement is larger than our threshold of 0.05 nm, the interval was identified as a discrete diffusion event. In similar fashion, a second diffusion event was identified forty picoseconds later. Note the large oscillations between the two diffusion events shown: while $\frac{dx'}{dt}$ exceeded the threshold on this interval, the oscillations did not result in significant net displacement, and were therefore discarded by our algorithm. Once this algorithm was applied to motion in the x, y, and z directions, any diffusion events that occurred at overlapping times were combined into a single diffusion event, and the instantaneous values were recorded in a discrete diffusion event dataset.

We should note that it is possible for the instantaneous positions recorded in the discrete diffusion dataset to correspond to displacements smaller than the threshold value of 0.05 nm. This possibility can arise for two reasons. First, displacements in all coordinates are recorded, even if (as is usually the case) displacement in only one coordinate triggered the algorithm to count the event as a discrete diffusion event. Second, we record instantaneous values, which are not identical to running mean values that are used to judge whether a discrete diffusion event has occurred.

The analysis of a discrete diffusion event was rationalized according to the sub-layer(s) of the QLL involved during the diffusion event. We have adopted here structural definitions introduced previously (ref. 16): admolecules are defined as water molecules located atop the outermost bilayer, designated ε_1 in Fig. 3. Beneath this sub-layer are

molecules belonging to the ε_2 sub-layer, which coincides with the pre-annealed outermost bilayer; this layer is more rigid and crystal-like compared to molecules located in the ε_1 sub-layer. Deeper bilayers are designated μ_1, μ_2, etc. Figure 3 also shows the well-known increase in QLL thickness with increasing temperature, which in turn implies an increase in the number of liquid-like molecules, N_{LL}.[17,52]

3. Results

3.1 Model independence of anisotropic diffusivity

Figure 4 displays results of Arrhenius analysis of diffusion coefficients of the three water-water models described above, obtained by application of Eqs. 1-5. The figure shows that, at low temperatures, diffusive anisotropy is manifest as a split between diffusion coefficient values in the x- and z-directions for any given model. For all models, and consistent with previous observation,[17] these differences indicate faster diffusion in the x-direction than in the z-direction (i.e., $D^*_x > D^*_z$), at low temperature. Quadratic functions of 1/T, best-fit to D_{xz}^*, are displayed as solid lines in Fig. 4: the non-linearity of the fit suggests a change in the diffusive mechanism moving from high to low temperatures. These fits exclude the lowest temperature data for TIP4P/2005 and TIP5P-Ew (-60 °C sub-melt temperature), which we regard as anomalously low outliers. Indeed, a sub-melt temperature of -60 °C corresponds to 192 K and 202 K (circled points in Fig. 4) for TIP4P/2005 and TIP5P-Ew, respectively, which are low in terms of absolute temperature. At such absolute temperatures the low values of D_x* and D_z* are due to an overestimation of the number of liquid-like molecules on the part of the tetrahedral method: surface molecules, even if tightly bound, cannot form a tetrahedral hydrogen-bonding geometry, as discussed by Gladich et al[17]. The result is Q-values that are unrealistically high, and thus values of D_x* and D_z* that are unrealistically low.

Characteristics of diffusion that reveal a transition from the low-temperature anisotropic diffusivity regime to the high-temperature isotropic diffusivity regime (the AI transition) are provided in Fig. 5. Figure 5a shows diffusion anisotropy ratios, D^*_x/D^*_z (or equivalently, D_x/D_z), derived from Fig. 4, as a function of the sub-melt temperature for all water models. The results show that the AI transition occurs at roughly the same range of sub-melt temperatures, around -35 °C. Although some uncertainty in the exact temperature of the transition is due to unavoidable statistical errors in the calculation of the diffusion coefficient at these low temperatures, the AI transition seems to be consistent among all water models and different slab dimensions. These uncertainties do not allow us to determine whether the AI transition is a sharp or smooth transition: longer simulations and finer temperature spacing are required to make this determination.

Figure 5b displays the enthalpy of activation for diffusion obtained from the slopes of the solid curve in Fig. 4, i.e. the best quadratic fit of D_{xz}^*. All of the intermolecular potentials exhibit increasing enthalpy of activation with rising temperature. Two of the models (NE6 and TIP5P-Ew) begin, at low temperature, at roughly one hydrogen bond.[17] Moreover, comparing slopes of the D^*_x and D^*_z curves in the low-temperature, anisotropic regime, we have found that the energy of activation in the x-direction differs from the energy of activation in the z-direction by less than 10%, for all models. This

suggests that the difference between the two in-plane diffusivities is unlikely to be due to differences in enthalpy, but rather by differences in entropy.

3.2 Statistics of discrete diffusion events

Following the procedure outlined in section 2.3, we identified 21782 discrete diffusion events over the duration of a simulation run of 100 ns. These were divided into categories according to starting and ending sub-layer (i.e., $\varepsilon_1 \rightarrow \varepsilon_1$, $\varepsilon_1 \rightarrow \varepsilon_2$, $\varepsilon_2 \rightarrow \varepsilon_1$, and $\varepsilon_2 \rightarrow \varepsilon_2$). As shown in Table 3, the vast majority of discrete diffusion events were found to correspond to motion within a given sub-layer: 75% of discrete diffusion events occurred as $\varepsilon_2 \rightarrow \varepsilon_2$, while 21% occurred as $\varepsilon_1 \rightarrow \varepsilon_1$. Inter-sub-layer diffusion events ($\varepsilon_1 \rightarrow \varepsilon_2$ and $\varepsilon_2 \rightarrow \varepsilon_1$) accounted for only 4% of the total.

The discrete diffusion dataset was also used to investigate the origin of anisotropy in the diffusion. The two predominant paired subsets ($\varepsilon_1 \rightarrow \varepsilon_1$ and $\varepsilon_2 \rightarrow \varepsilon_2$) were used to construct joint displacement histograms (Fig. 6) using a bin width of 0.015 nm in both directions. Comparison of Figs. 6a and 6b shows that the anisotropy in the diffusion is almost entirely due to motion within the $\varepsilon_1 \rightarrow \varepsilon_1$ sub-layer. Moreover, Fig. 6a also shows that displacements are concentrated along the horizontal axis (x-direction) within the range of 0.1 to 0.6 nm. These distances correspond to interstitial motions in the x-direction. Figure 6a also displays bands of much larger displacement in the z-direction ($\Delta z \sim \pm 0.8$ nm), which also correspond to interstitial jump distances; however, these displacements are much less frequent than displacements in the x-direction.

Discrete diffusion events belonging to each sub-layer combination were averaged to obtain a sub-layer-specific, event-mean diffusivity. For example, molecules jumping from ε_1 to ε_2, traversing a distance Δx in the process, would contribute to an event-mean diffusivity designated as $\langle(\Delta x)^2\rangle_{\varepsilon_1 \rightarrow \varepsilon_2}$. Ratios between these quantities for a given sub-layer transition are used to calculate an event-mean anisotropy, designated $A_{x/z}$. For example, the event-mean anisotropy for $\varepsilon_1 \rightarrow \varepsilon_2$ is given by

$$A_{x/z}(\varepsilon_1 \rightarrow \varepsilon_2) = \frac{\langle(\Delta x)^2_{\varepsilon 1 \rightarrow \varepsilon 2}\rangle}{\langle(\Delta z)^2_{\varepsilon 1 \rightarrow \varepsilon 2}\rangle} \quad (6)$$

Results are displayed in Table 3. Although the preponderance (75%) of discrete diffusion events occur as $\varepsilon_2 \rightarrow \varepsilon_2$, these events exhibit a smaller event-mean diffusivity compared to $\varepsilon_1 \rightarrow \varepsilon_1$ because the average jump distance is much smaller. Finally, we note that the isotropy of $\varepsilon_2 \rightarrow \varepsilon_2$ diffusion evident in Fig. 6 appears quantitatively in Table 3 with a value of $A_{x/z}$ close to unity; on the other hand the anisotropy of $\varepsilon_1 \rightarrow \varepsilon_1$ diffusion in Fig. 6 appears here with a value of $A_{x/z}$ close to two.

We also used the discrete diffusion dataset to investigate the mechanism of diffusion. Specifically, we gauged the occurrence of concerted exchange diffusion within the predominant paired subset ($\varepsilon_1 \rightarrow \varepsilon_1$), according to the following algorithm. For a given discrete diffusion event, if a molecule registered a minimum displacement (d_{min}), and a

second molecule exchanged places with it within a given tolerance in time (t_{min}) and position (p_{min}), the event was judged to be an exchange. The values used for these tolerances, p_{min} = 0.15 nm and t_{min} = 30 ps, are intentionally generous: observed thermal displacements are well within p_{min} at this temperature, for example. (The estimated thermalization time is derived from a previous estimate of the surface thermalization time of 10 ps at 250 K,[24] corrected to the simulation temperature of 230 K by multiplying by an Arrhenius factor based on an estimated enthalpy of thermalization of one hydrogen bond, hence $\exp(\frac{25\ \mathrm{kJ/mol}}{R}\left(\frac{1}{230}-\frac{1}{250}\right)) \approx 3$). The minimum displacement value used, d_{min} = 0.3 nm, is similarly generous in the sense that it is only slightly larger than the thermal displacement tolerance (p_{min}), but still smaller than expected interstitial displacements at the prismatic ice surface. The results indicate that exchange explains less than ~10% of the total diffusion within $\varepsilon_1 \rightarrow \varepsilon_1$. Increasing the tolerances by 50% does not alter this conclusion. These results indicate that the predominant mechanism for diffusion is by uncorrelated hopping, or jumping.

3.3 Atomistic mechanism of anisotropic diffusivity of NE6 water ice within ε_1

We next investigate the molecular-level mechanism for $\varepsilon_1 \rightarrow \varepsilon_1$ diffusion in the low-temperature (anisotropic) diffusion regime for the NE6 model. Fig. 7a shows a representative snapshot looking down on the prismatic surface, suggesting that ε_1 admolecules possess a distinct preference for interstitial positions with respect to the underlying crystal lattice in the z-direction. That is to say, the jumping-off position for admolecules diffusing at temperatures below the AI transition is interstitial. Fig. 7b displays a two-dimensional histogram obtained by collecting the horizontal position of all ε_1 molecules during the NE6 trajectory computed at -49□C sub-melt temperature (240 K), over a period of 200 ns. This two-dimensional histogram, which serves as a probability density function, $\rho(x,z)$, of molecules in the ε_1 sub-layer, indicates the same strong selectivity for the interstitial configuration of the ε_1 sub-layer as suggested by Fig. 7a.

Figure 8 shows relative Gibbs energies as functions of x and z. Each function was obtained by averaging over a narrow window in the orthogonal in-plane direction,

$$\Delta G(x) = -RT\ln(\langle\rho\rangle_z) \quad (7a)$$

$$\Delta G(z) = -RT\ln(\langle\rho\rangle_x) \quad (7b)$$

where brackets indicate an average over the indicated range (see the outlined boxes in Fig. 7b). The function $\Delta G(x)$ (Fig. 8a) exhibits a repeating pattern of doublet minima. The molecular orientation of an ε_1 molecule in this position is depicted in the adjoining molecular snapshot (drawn below the function); this orientation is an interstitial position above the lattice. The other minimum of the doublet is separated from this one by a Gibbs energy barrier of ~2 kJ/mol. Since RT at this temperature is ~2 kJ/mol (assuming a sub-melt temperature of -49 degrees, or 240 K), this is a mildly suprathermal barrier: transitions of this type will likely appear as thermal noise in trajectory calculations, and will not be identified as discrete diffusion events according to the algorithm described in

section 2.3. On the other hand, each doublet is separated from the next by a barrier of $\Delta G_x^+ \approx 10\ kJ/mol$. Since this barrier is considerably more suprathermal, transitions of this type will likely be identified as discrete diffusion events.

The function *ΔG(z)* (Fig. 8b) reveals troughs separated from one another by a barrier of $\Delta G_z^+ \approx 12\ kJ/mol$. Molecular orientations associated with two such admolecules are depicted in the adjoining molecular snapshot. Transitions between adjacent troughs will also likely appear as discrete diffusion events in trajectory calculations.

Figures 7-8 were constructed based on the rectangular (NE6) slab, but results for the square NE6(sq) slab (not shown) are in all important respects the same.

These observations motivate the following mechanistic inferences regarding NE6:

1. Diffusion in both in-plane directions occurs via a jumping mechanism. The transition state of jumps is entropically favored over the starting, metastable interstitial position. This follows from consideration of the observation that the Gibbs energy barriers of 10 and 12 kJ/mol for diffusion in the x- and z- directions are smaller than Arrhenius enthalpies of activation presented in Fig. 5b. This inference also makes intuitive sense: as an interstitial water molecule moves to a transition state, it loses one hydrogen bond, and thereby acquires increased freedom of motion.

2. Transition states in the two in-plane directions possess different entropies relative to the metastable interstitial position. Indeed, as we comment above concerning Fig. 5b and consistently with results reported elsewhere,[17] the enthalpy of activation is not significantly different in the two in-plane directions. Thus, we can ascribe the difference in activation Gibbs energy between the two in-plane directions to entropy,

$$(\Delta G_x^+ - \Delta G_z^+) = -T(\Delta S_x^+ - \Delta S_z^+) \quad (9)$$

   which yields $\Delta S_x^+ - \Delta S_z^+ \approx 8$ J mol^{-1}K^{-1} at 240 K. (For comparison, the calculated residual entropy of disordered ice is 3.4 J mol^{-1}K^{-1}.[53,54])

3. As noted above, the nonlinearity of the Arrhenius plot suggests that the system evolves from predominance of one diffusion mechanism to another, as a function of temperature.

4. Discussion

The results presented here suggest a framework for understanding the AI transition, as follows. Diffusion in the low-temperature, anisotropic regime is characterized by low enthalpy of activation (on the order of one hydrogen bond or less), and is comprised of motion mainly within the upper (ε_1) sub-layer. Diffusion is anisotropic in this regime because of a difference in the entropy of transition states to motion in the x- and z-direction. Above the AI transition temperature, an isotropic mechanism begins to

dominate the diffusion. This occurs because the difference in energy barriers become less significant compared to temperature, and (as Fig. 5b shows) diffusion in this regime is characterized by higher enthalpy of activation (on the order of two hydrogen bonds), and is comprised of motion mainly within the lower (ε_2) sub-layer. In fact, as temperatures approach the melting point, the distinction between sub-layers ε_1 and ε_2, and indeed deeper layers μ_1, μ_2, etc., becomes less meaningful because of increasingly rapid molecular exchange between layers, and because of increasing fluctuations of the instantaneous local order.[55] The considerable thickness of the QLL at higher temperature suggests that diffusion will become similar to diffusion in bulk supercooled water; indeed, experiment indicates an energy of activation in bulk supercooled water on the order of two hydrogen bonds at 238 K.[41] This framework also explains the increase in enthalpy of activation with temperature shown in Fig. 5b.

Although not previously described for water ice, several aspects of this explanation appear in the context of metal epitaxy, where monolayer islands on anisotropic metal crystal facets have been well-documented.[18,56,57] In particular, a close analogy exists in the case of surface self-diffusivity atop the Ni(110) surface: an AI transition in this system has been described in terms of two distinct molecular diffusion mechanisms, one anisotropic and the other isotropic, the latter overtaking the former at high temperature owing to its larger energy of activation.[56,58]

The same type of analysis as conducted in section 3.3 could in principle be repeated for TIP4P/2005 and TIP5P-Ew, in order to also obtain a 2D free energy profile for the position of ε_1 molecules on the top of ε_2 sub-layers. However, for these models, we have found that it is extremely difficult to obtain meaningful statistics from trajectories of only 200 ns. Indeed, for similar sub-melting temperatures (-50 °C), the corresponding absolute temperature is much lower: 202 K and 221 K for TIP4P/2005 and TIP5P-Ew, respectively, compared to 240 K for NE6. Since the diffusivity is function of the sub-melting as well as of the absolute temperature, the low temperatures for TIP4P/2005 and TIP5P-Ew resulted in poor statistics, which prevented the creation of meaningful 2D free energy profiles. Moreover, the 2D free energy profile for NE6 was created based on a structural criterion to distinguish ε_1 and ε_2 molecules, i.e., assuming a flat separation between sub-layers. Interestingly, especially at these low temperatures, we have found large lateral inhomogeneities in the QLL for TIP4P/2005 and TIP5P-Ew, preventing the creation of the 2D histograms. This finding raises new questions and promises new intercomparison studies.

The precision with which we can meaningfully assign the AI transition temperature is constrained by the gradual nature of the change in anisotropy presented in Fig. 5, perhaps ±10°C. One source of uncertainty is computational noise: obtaining statistical properties from MD at low temperature is difficult because extremely long trajectories are needed to obtain secure statistics. Nor can we rule out a second possibility, namely that the transition is intrinsically gradual. Unfortunately, experimental uncertainties in diffusion on ice are too large to permit resolution of this matter.[59] Additional experimental and computational work is needed to address this question.

5. Conclusions

The results presented here support the proposition that an anisotropic-to-isotropic temperature threshold characterizes surface self-diffusion on prismatic ice-vapor interfaces. Below this threshold, this anisotropy is such that diffusion in the direction parallel to the crystallographic a-axis is faster than in the direction parallel to the crystallographic c-axis; the threshold occurs consistently across three distinct representations of the water-water intermolecular potential, at a sub-melt temperature centered at -35 °C. Mechanistically, we find that the low-temperature anisotropic diffusion regime can be understood in terms of mobile interstitial admolecules which, hopping across a landscape that is rigid with respect to the diffusion time scale, sense the symmetry of the underlying crystalline lattice, and hence face entropically distinct barriers to motion in the two in-plane directions. Above the AI transition temperature, diffusion transitions to a mechanism that begins to engage the entire QLL as a fluid, characterized by higher energy barriers that are more isotropic in the in-plane direction, and less sensitive to the symmetry of the underlying crystalline lattice. While this explanation has not previously been applied to water ice, close analogies exist in surface self-diffusion on metal facets.

6. Acknowledgements

S.N. was supported by NSF grant award CHE-1306366 for this work. P.R. received support from NSF award ARC-1108451 and from USACH-DICYT 041331CC_DAS. M.R. was supported by the Czech Science Foundation via grant no. 13-06181S. We also thank Vladimir Spirko, Pavel Jungwirth, and Marcelo Carignano for their thoughtful reading and feedback on parts of this manuscript, which greatly improved it. The authors dedicate this paper in fond memory of co-author Martina Roeselova: a great teacher and scientist, but above all, a dear and real friend. Thank you, Martina.

7. References

1 A. J. Baran, *J. Quant. Spectrosc. Radiat. Transf.*, 2009, **110**, 1239–1260.

2 P. Yang, G. Hong, G. W. Kattawar, P. Minnis and Y. Hu, *Geosci. Remote Sens. IEEE Trans. On*, 2008, **46**, 1948–1957.

3 S. P. Neshyba, B. Lowen, M. Benning, A. Lawson and P. M. Rowe, *J. Geophys. Res. Atmospheres*, 2013, **118**, 3309–3318.

4 V. Shcherbakov, J. F. Gayet, O. Jourdan, J. Ström and A. Minikin, *Geophys. Res. Lett.*, 2006, **33**, L15809.

5 A. J. Baran, *Atmospheric Res.*, 2012, **112**, 45–69.

6 Z. Ulanowski, E. Hesse, P. H. Kaye and A. J. Baran, *J. Quant. Spectrosc. Radiat. Transf.*, 2006, **100**, 382–392.

7 J. S. Wettlaufer, *Philos. Trans. R. Soc. Lond. Ser. Math. Phys. Eng. Sci.*, 1999, **357**, 3403–3425.

8 J. P. Van der Eerden, *Handb. Cryst. Growth*, 1993, **1**, 307–475.

9 A. A. Chernov, *Modern crystallography*, Springer, 1984.

10 C. D. Westbrook, A. J. Illingworth, E. J. O'Connor and R. J. Hogan, *Q. J. R. Meteorol. Soc.*, 2010, **136**, 260–276.

11 C. Zhou, P. Yang, A. E. Dessler and F. Liang, *Geosci. Remote Sens. Lett. IEEE*, 2013, **10**, 986–990.

12 Z. Ulanowski, P. H. Kaye, E. Hirst, R. S. Greenaway, R. J. Cotton, E. Hesse and C. T. Collier, *Atmos Chem Phys*, 2014, **14**, 1649–1662.

13 U. Nakaya, *Snow crystals: natural and artificial*, Harvard University Press, 1954.

14 D. Kuroiwa, *J Glaciol*, 1969, **8**, 475–483.

15 W. C. Pfalzgraff, R. M. Hulscher and S. P. Neshyba, *Atmos Chem Phys*, 2010, **10**, 2927–2935.

16 W. Pfalzgraff, S. Neshyba and M. Roeselova, *J. Phys. Chem. A*, 2011.

17 I. Gladich, W. Pfalzgraff, O. Maršálek, P. Jungwirth, M. Roeselová and S. Neshyba, *Phys Chem Chem Phys*, 2011, **13**, 19960–19969.

18 H. Brune, *Surf. Sci. Rep.*, 1998, **31**, 125–229.

19 Y. Saitō, *Statistical physics of crystal growth*, World Scientific, 1996.

20 K. Bolton and J. B. C. Pettersson, *J. Phys. Chem. B*, 2000, **104**, 1590–1595.

21 J. P. D. Abbatt, J. L. Thomas, K. Abrahamsson, C. Boxe, A. Granfors, A. E. Jones, M. D. King, A. Saiz-Lopez, P. B. Shepson, J. Sodeau, D. W. Toohey, C. Toubin, R. von Glasow, S. N. Wren and X. Yang, *Atmospheric Chem. Phys.*, 2012, **12**, 6237–6271.

22 C. L. Bishop, D. Pan, L. M. Liu, G. A. Tribello, A. Michaelides, E. G. Wang and B. Slater, *Faraday Discuss*, 2008, **141**, 277–292.

23 M. Watkins, D. Pan, E. G. Wang, A. Michaelides, J. VandeVondele and B. Slater, *Nat. Mater.*, 2011, **10**, 794–798.

24 S. Neshyba, E. Nugent, M. Roeselová and P. Jungwirth, *J. Phys. Chem. C*, 2009, **113**, 4597–4604.

25 M. M. Conde, C. Vega, A. Patrykiejew and others, *J. Chem. Phys.*, 2008, **129**, 14702–14702.

26 T. D. Shepherd, M. A. Koc and V. Molinero, *J. Phys. Chem. C*, 2012, **116**, 12172–12180.

27 R. Ferrando, *Phys. Rev. Lett.*, 1996, **76**, 4195–4198.

28 F. Montalenti and R. Ferrando, *Phys. Rev. B*, 1999, **59**, 5881.

29 H. Nada and J. P. J. M. van der Eerden, *J. Chem. Phys.*, 2003, **118**, 7401.

30 J. L. F. Abascal and C. Vega, *J. Chem. Phys.*, 2005, **123**, 234505.

31 S. W. Rick, *J. Chem. Phys.*, 2004, **120**, 6085–6093.

32 M. A. Carignano, P. B. Shepson and I. Szleifer, *Mol. Phys.*, 2005, **103**, 2957–2967.

33 A. Reinhardt, J. P. K. Doye, E. G. Noya and C. Vega, *J. Chem. Phys.*, 2012, **137**, 194504.

34 E. Sanz, C. Vega, J. R. Espinosa, R. Caballero-Bernal, J. L. F. Abascal and C. Valeriani, *J. Am. Chem. Soc.*, 2013, **135**, 15008–15017.

35 R. G. Pereyra, I. Szleifer and M. A. Carignano, *J. Chem. Phys.*, 2011, **135**, 034508.

36 R. G. Fernández, J. L. Abascal and C. Vega, *J. Chem. Phys.*, 2006, **124**, 144506.

37 C. Vega, J. L. F. Abascal, M. M. Conde and J. L. Aragones, *Faraday Discuss.*, 2008, **141**, 251–276.

38 C. Vega, J. L. F. Abascal and P. G. Debenedetti, *Phys. Chem. Chem. Phys.*, 2011, **13**, 19660–19662.

39 J. L. F. Abascal, R. G. Fernández, C. Vega and M. A. Carignano, *J. Chem. Phys.*, 2006, **125**, 166101.

40 H. L. Pi, J. L. Aragones, C. Vega, E. G. Noya, J. L. F. Abascal, M. A. Gonzalez and C. McBride, *Mol. Phys.*, 2009, **107**, 365–374.

41 W. S. Price, H. Ide and Y. Arata, *J. Phys. Chem. A*, 1999, **103**, 448–450.

42 V. Buch, P. Sandler and J. Sadlej, *J. Phys. Chem. B*, 1998, **102**, 8641–8653.

43 C. Vega, M. Martin-Conde and A. Patrykiejew, *Mol. Phys.*, 2006, **104**, 3583–3592.

44 B. Hess, C. Kutzner, D. Van Der Spoel and E. Lindahl, *J. Chem. Theory Comput.*, 2008, **4**, 435–447.

45 R. W. Hockney, S. P. Goel and J. W. Eastwood, *J. Comput. Phys.*, 1974, **14**, 148–158.

46 U. Essmann, L. Perera, M. L. Berkowitz, T. Darden, H. Lee and L. G. Pedersen, *J. Chem. Phys.*, 1995, **103**, 8577–8593.

47 T. Darden, D. York and L. J. Pedersen, *J Chem Phys*, 1993, **98**, 10089–10092.

48 G. Bussi, D. Donadio and M. Parrinello, *J. Chem. Phys.*, 2007, **126**, 014101.

49 M. Parrinello and A. Rahman, *J. Appl. Phys.*, 1981, **52**, 7182–7190.

50 S. Miyamoto and P. A. Kollman, *J. Comput. Chem.*, 1992, **13**, 952–962.

51 J. R. Errington and P. G. Debenedetti, *Nature*, 2001, **409**, 318–321.

52 I. Gladich and M. Roeselová, *Phys. Chem. Chem. Phys.*, 2012, **14**, 11371–11385.

53 V. F. Petrenko and R. W. Whitworth, *Physics of Ice*, Oxford University Press, 1999.

54 L. Pauling, *J. Am. Chem. Soc.*, 1935, **57**, 2680–2684.

55 D. C. David T. Limmer, *J. Chem. Phys.*, 2014, **141**.

56 E. E. Latta and H. P. Bonzel, *Phys. Rev. Lett.*, 1977, **38**, 839–841.

57 E. Preuss, N. Freyer and H. P. Bonzel, *Appl. Phys. A*, 1986, **41**, 137–143.

58 H. P. Bonzel and E. E. Latta, *Surf. Sci.*, 1978, **76**, 275–295.

59 O. B. Nasello, S. Navarro de Juarez and C. L. Di Prinzio, *Scr. Mater.*, 2007, **56**, 1071–1073.

60 K. G. Libbrecht, *J. Cryst. Growth*, 2003, **247**, 530–540.

61 K. G. Libbrecht, *Arxiv Prepr. ArXiv08100689*, 2008.

62 G. S. Bales and A. Zangwill, *Phys. Rev. B*, 1990, **41**, 5500–5508.

63 V. F. Petrenko, *Structure of Ordinary Ice Ih. Part 1: Ideal Structure of Ice*, DTIC Document, 1993.

Table 1: Water force field parameters: oxygen-hydrogen distance (d_{OH}) hydrogen-oxygen-hydrogen angle (HOH), Lennard-Jones parameters (σ and ε), charges on oxygen (q_O), hydrogen (q_H) and massless sites (q_M and q_L), oxygen-M-site and oxygen –L-site distances (d_{OM} and d_{OL} respectively).

MODEL	d_{OH} (Å)	HOH (°)	σ (Å)	ε(kJ mol^{-1})	q (e)	q_H (e)	q_M (e)	q_L (e)	d_{OM} (Å)	d_{OL} (Å)
TIP4P/2005	0.9572	104.52	3.1589	0.77490	0	0.5564	-1.1128	—	0.1546	—
TIP5P-Ew	0.9572	104.52	3.0970	0.74480	0	0.241	—	-0.241	—	0.7
NE6	0.980	108.00	3.115(O) 0.673(H)	0.714850(O) 0.115419(H)	0	0.477	-0.866	-0.044	0.230	0.8892

Table 2: Melting temperatures for TIP4P/2005, TIP5P-Ew and NE6 water models, including the experimental reference value.

MODEL	T_m (K)
TIP4P/2005	252 [30,36]
TIP5P-Ew	272 [36]
NE6	289 [39]
Exp.	273.15

Table 3. Event-mean anisotropies.

Transition	Events (%)	$\langle(\Delta x)^2\rangle$	$\langle(\Delta z)^2\rangle$	$A_{x/z}$
$\varepsilon_1 \rightarrow \varepsilon_1$	21	0.0725	0.0389	1.9
$\varepsilon_2 \rightarrow \varepsilon_2$	75	0.0168	0.0172	1.0
$\varepsilon_1 \rightarrow \varepsilon_2$	2	0.1735	0.1412	1.2
$\varepsilon_2 \rightarrow \varepsilon_1$	2	0.1648	0.1462	1.1

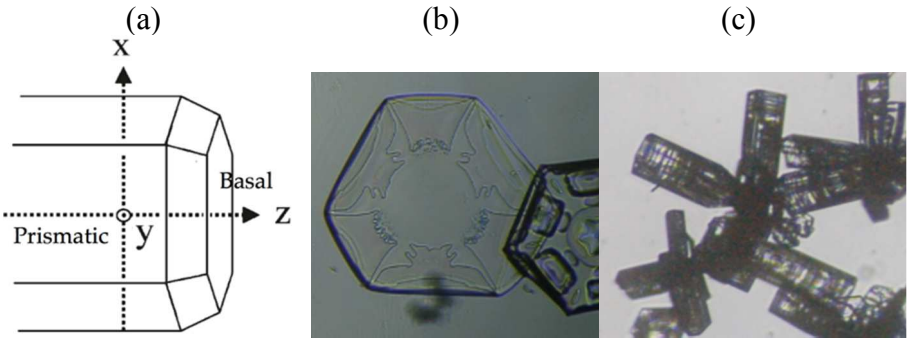

Figure 1. (a) Schematic of a hexagonal ice prism indicating definitions of coordinates used in this paper.[63] Coordinate z coincides with the vector perpendicular to the basal (0001) facet (i.e., the crystallographic c-axis); coordinate y coincides with the vector perpendicular to the prismatic $(10\bar{1}0)$ facet; and coordinate x coincides with the vector [perpendicular to the secondary prismatic $(11\bar{2}0)$ facet. (b) Optical photograph of hexagonal plates recorded at Summit, Greenland on 31 August 2012 (temperature -17 □C, 91% relative humidity), supplied courtesy of Chris Cox (personal communication). (c) Optical photograph of a cluster of hexagonal columns recorded at Summit, Greenland on 2 December 2013 (-52 □C, 57% relative humidity), supplied courtesy of Von Walden (personal communication).

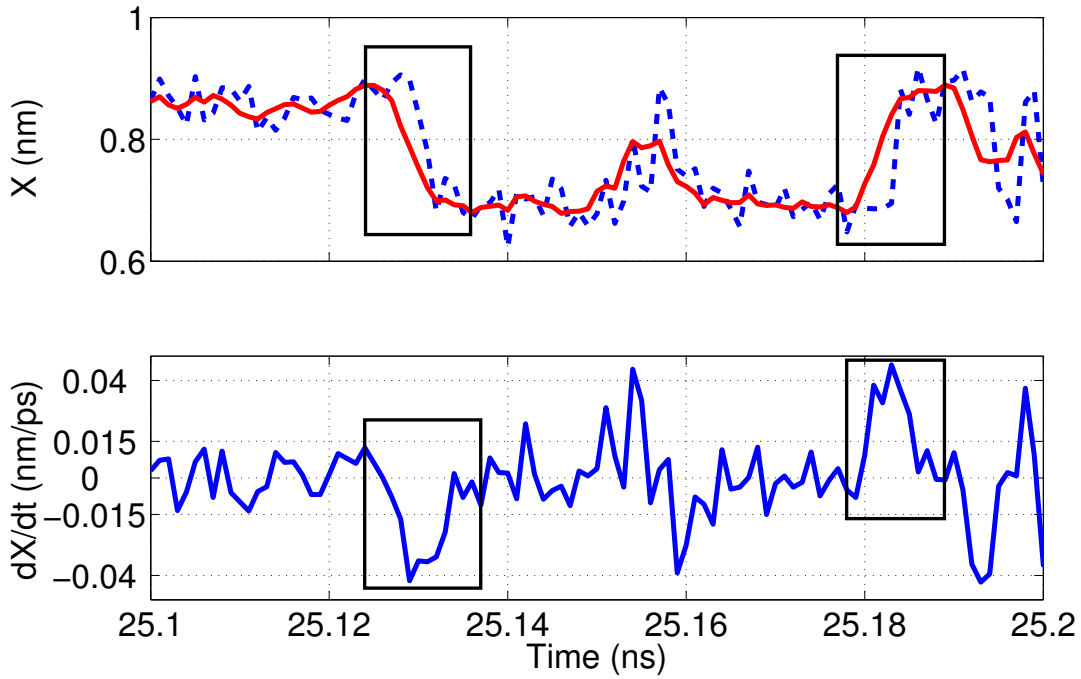

Figure 2. Trajectory of a water molecule at the surface of an NE6 slab at a sub-melt temperature of -59°C (230 K). The dashed blue line in the upper panel shows the *x*-coordinate of the oxygen atom of the molecule at the MD-recorded time resolution (1 ps); the solid red line shows its five-picosecond running mean (x', designated generically as s' in section 2.3). The lower panel shows the numerical first derivative of the running mean, ($\frac{dx'}{dt}$, designated generically as $\frac{ds'}{dt}$). Discrete diffusion events identified by the algorithm described in section 2.3 are highlighted in boxes.

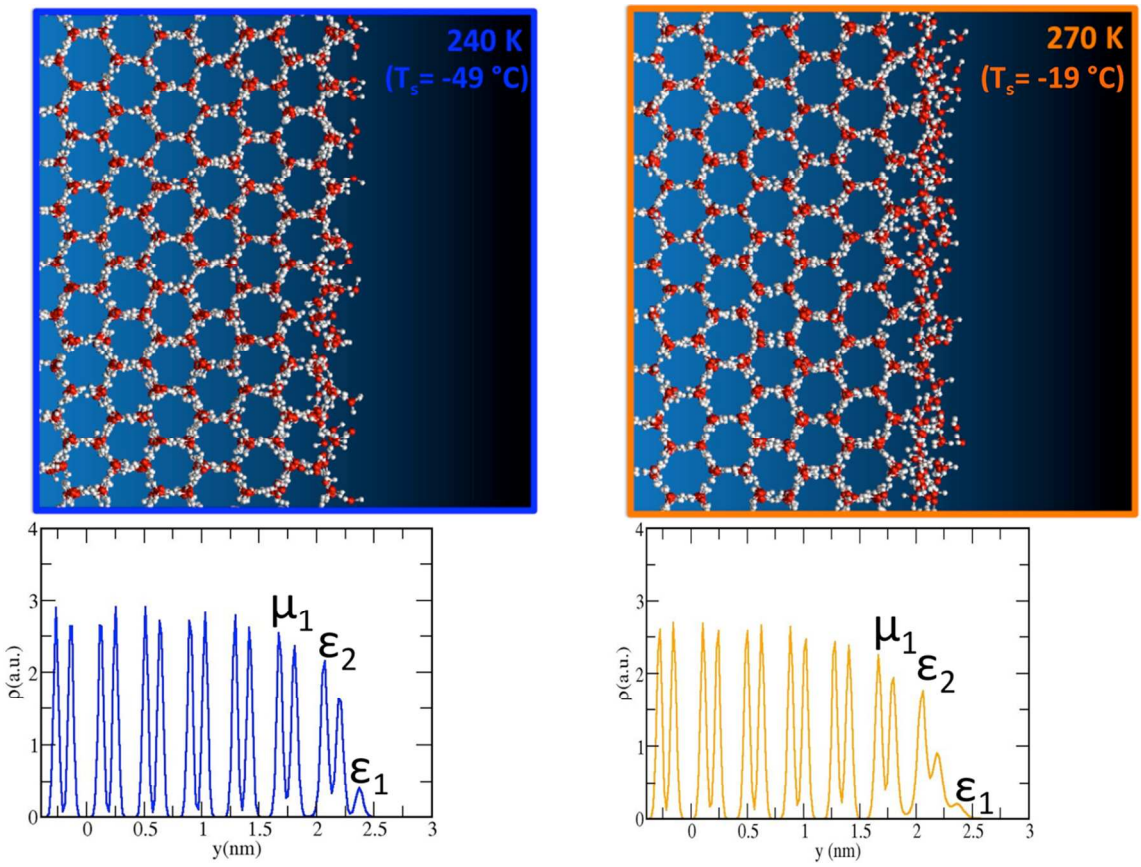

Figure 3. Upper panels: snapshots of NE6 water slabs at two temperatures showing increase in thickness of the quasi-liquid layer with increasing temperature. Lower panels: density profiles of oxygen atoms as a function of the y-coordinate (i.e., integrated over coordinates x and z), aligned with the overlying snapshots. The outermost part of the surface bilayer is designated sub-layer ε_1, and is comprised of highly mobile and mostly interstitial admolecules. To the left of ε_1 lies sub-layer ε_2, which is comprised of molecules less mobile molecules found mainly in lattice positions. To the left of ε_2 lies the even less mobile and more structured bilayer μ_1.

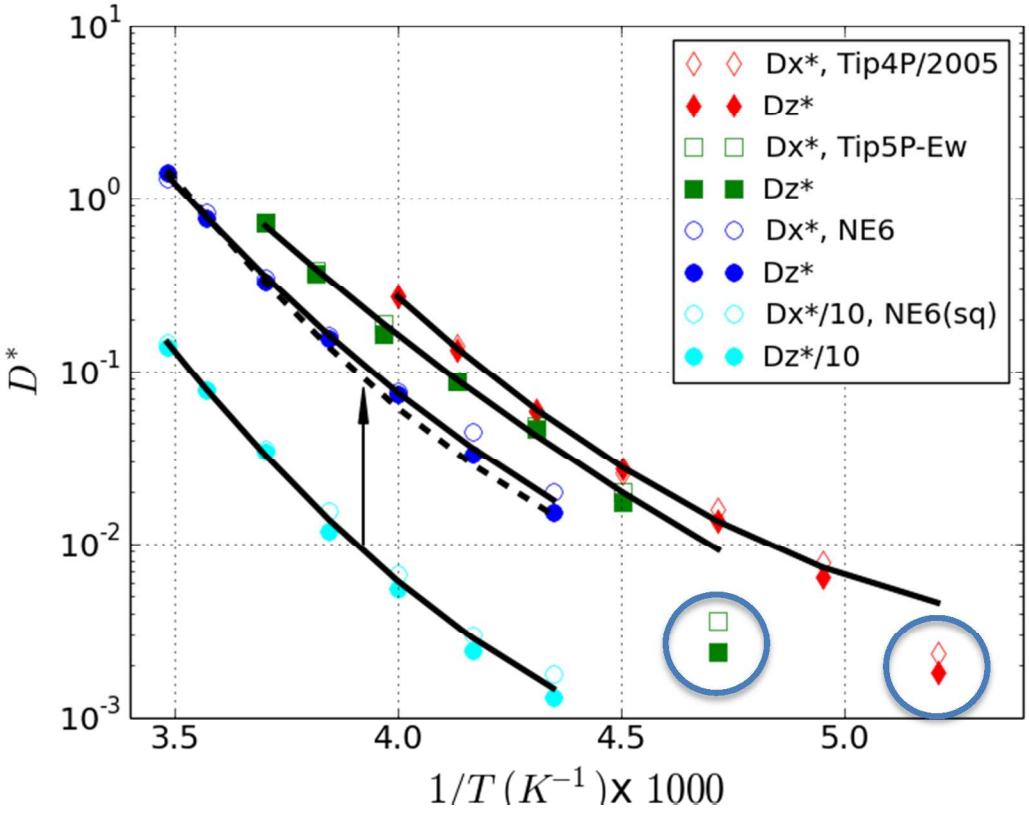

Figure 4. Arrhenius plot of scaled surface self-diffusion coefficients (Eq. 3). Error bars corresponding to one standard deviation are on the order of the size of the symbols, or smaller. Pairs of open and filled markers for each model at a given temperature indicate D_x* and D_z*. Where significant vertical separation between these markers occurs, anisotropic diffusion is inferred; examples of anisotropic diffusion for low-temperature Tip4P/2005 and Tip5P-Ew are highlighted with circles. Solid lines are based on a quadratic best-fit line to geometric averages of D_x* and D_z* for each model, omitting the lowest-temperature values for Tip4P/2005 and Tip5P-Ew. For visibility, values for the nearly square slab of NE6 (designated NE6(sq)) are displaced downward by a factor of 10; the proper location of these values on the graph is indicated by the dashed line.

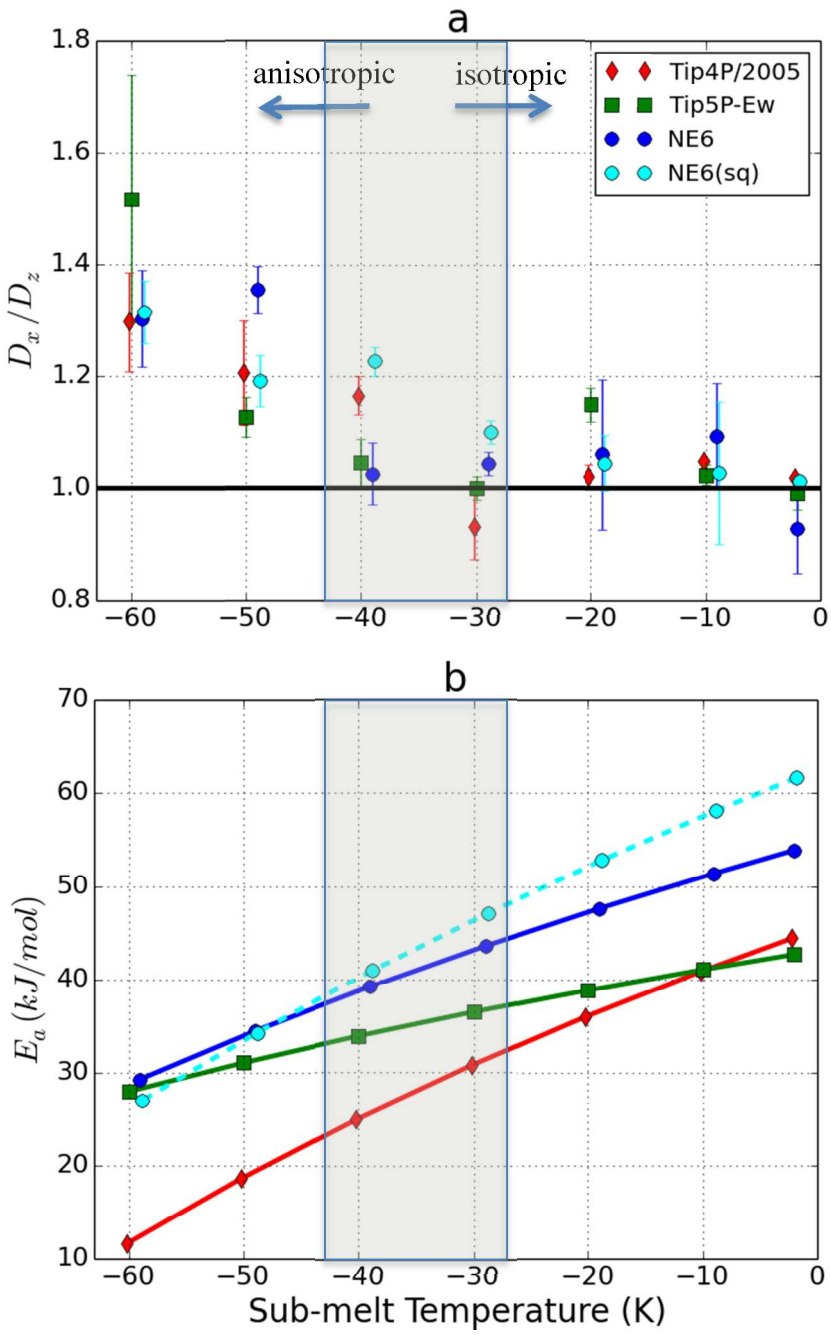

Figure 5. (a) Surface self-diffusion anisotropy ratio as a function of sub-melting temperature, for three model representations of water, obtained from Fig. 4. Sub-melt temperature is defined as $T_{simulation}$-T_{melt}, where T_{melt} equals 253 K for Tip4P/2005,[30] 272 K for Tip5P-Ew,[36] and 289 K for NE6.[39] Error bars are reported as one standard deviation, propagating the statistical uncertainty on the diffusion coefficient D_x and D_z provided by GROMACS.[44] The bold horizontal line demarcates a ratio of one, i.e. isotropic self-diffusion. (b) Enthalpy of activation derived from Fig. 4. Shaded area indicates the AI transition temperature range.

(a)

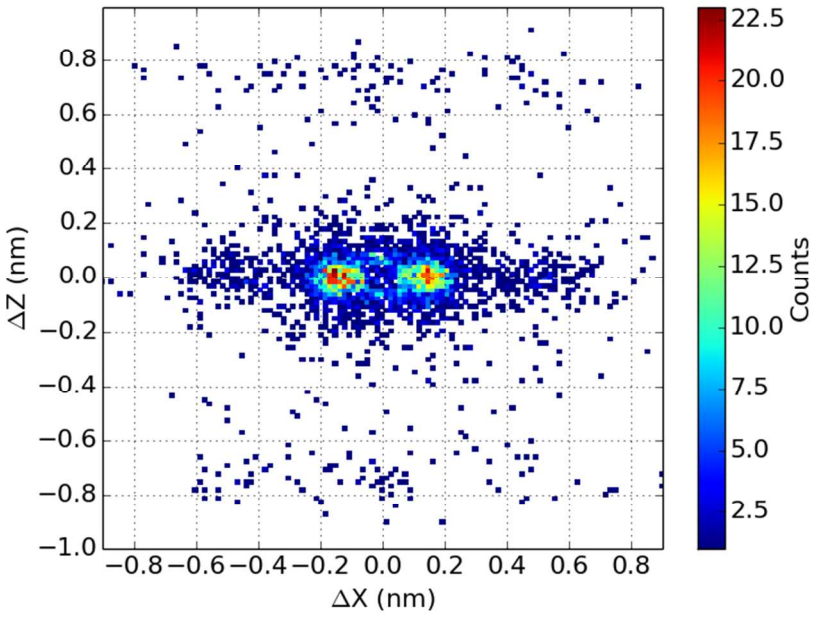

(b)

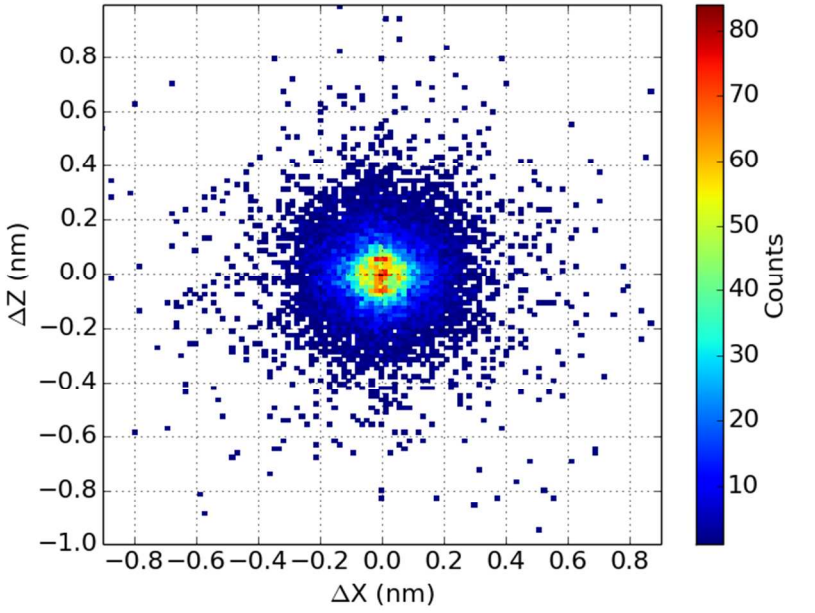

Figure 6. Joint displacement histograms for subsets belonging to $\varepsilon_1 \rightarrow \varepsilon_1$ (a) and $\varepsilon_2 \rightarrow \varepsilon_2$ (b) for 30 ns simulation. As noted in section 2.3, because the discrete diffusion events in any of the three Cartesian directions can trigger a diffusion event, and because instantaneous values (rather than the mean 5 ps running mean values) are recorded, displacements smaller than the threshold value of 0.05 nm appear.

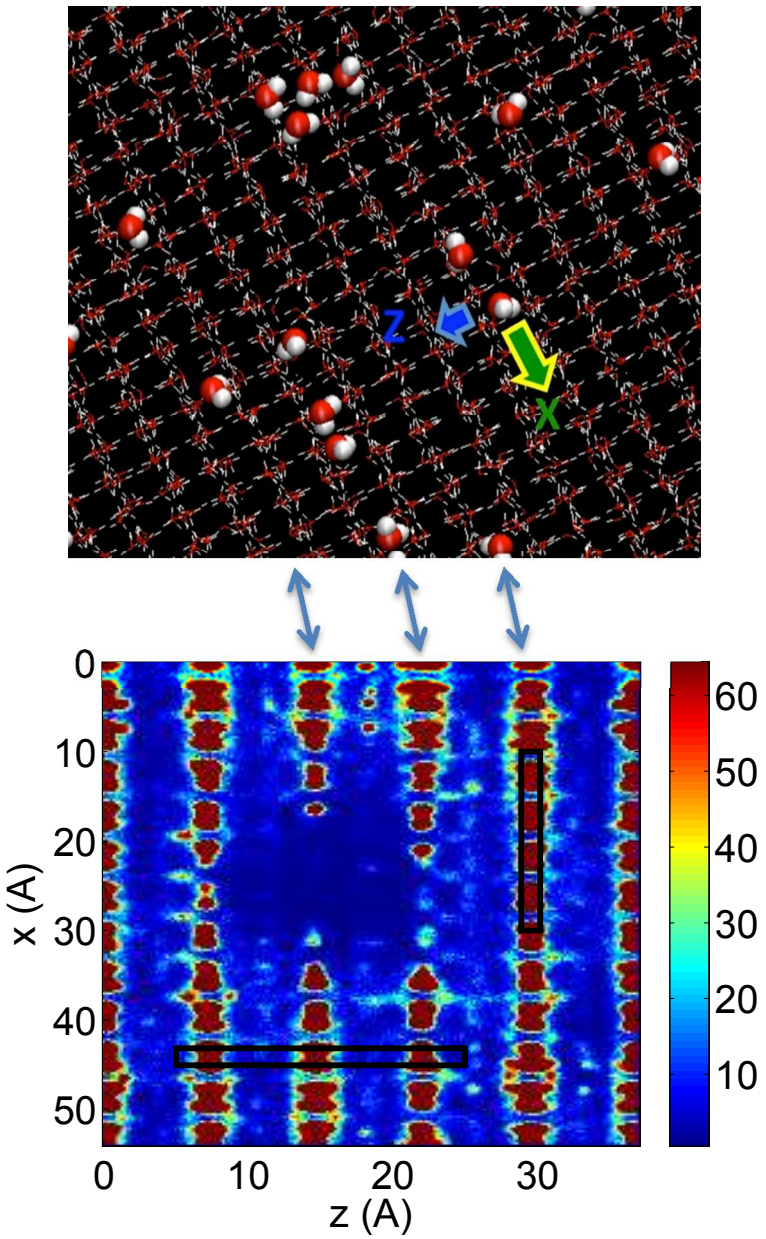

Figure 7. (a) Plan view of the exposed prismatic facet with admolecules (ε_1 sub-layer) designated by space-filled models. Preference of admolecules for interstitial positions is evident from the observation that nearly all appear to lie between lattice positions populated by the underlying ice molecules, which are designated by licorice models. (b) Plan view of the probability distribution function, $\rho(x,z)$, of ε_1 molecules in an NE6 slab at -49□C sub-melt temperature (240 K), over a 100 ns period, using bins with edge lengths 0.27 Å and 0.18 Å in x and z, respectively. The color bar indicates ε_1 molecules per bin accumulated over the trajectory. Rectangular boxes outline regions used for Gibbs energy profiles along the long edge of each box.

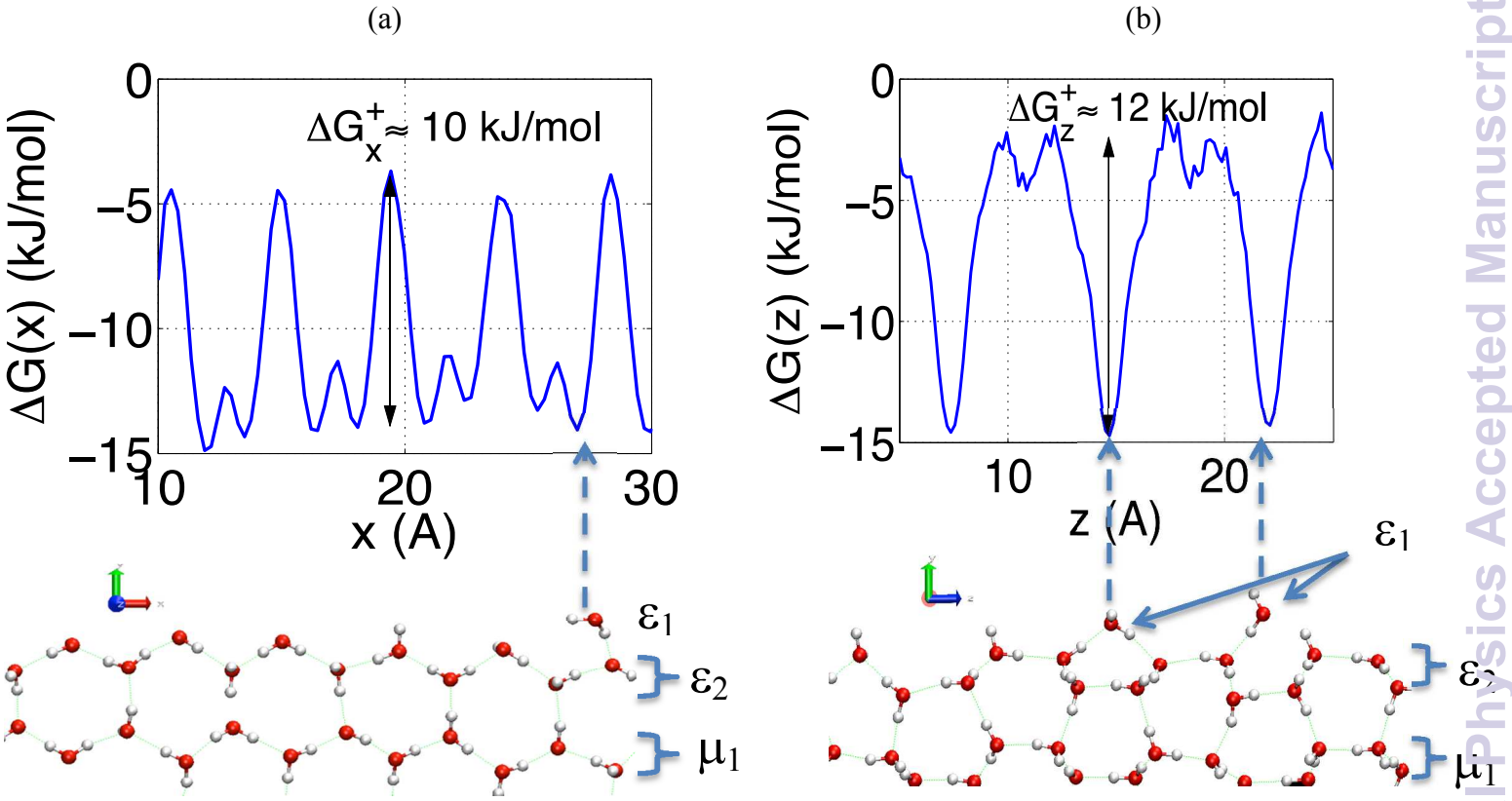

Figure 8. Gibbs energy profiles and snapshots of simulation results in the x-direction (a) and z-direction (b), derived from Fig. 7 using Eqs. 7 and 8.